Heterogeneous MEMS device assembly and integration

Patrice Topart[a1], Francis Picard[a], Samir Ilias[a], Christine Alain[a], Claude Chevalier[a], Bruno Fisette[a], Jacques E. Paultre[a], Francis Généreux[a], Mathieu Legros[a], Jean-F. Lepage[b], Christian Laverdière[b], Linh N. Phong[c], Jean-Sol Caron[a] and Yan Desroches[a]
[a] INO, 2740, Einstein Street, Québec, Québec, Canada, G1P 4S4
[b] Defence Research and Development Canada, 2459, de la Bravoure road, Québec, Canada
[c]Canadian Space Agency, 6767 route de l'Aéroport, Saint-Hubert, QC J3Y 8Y9, Canada

ABSTRACT

In recent years, smart phone applications have both raised the pressure for cost and time to market reduction, and the need for high performance MEMS devices. This trend has led the MEMS community to develop multi-die packaging of different functionalities or multi-technology (i.e. wafer) approaches to fabricate and assemble devices respectively. This paper reports on the fabrication, assembly and packaging at INO of various MEMS devices using heterogeneous assembly at chip and package-level. First, the performance of a giant (e.g. about 3 mm in diameter), electrostatically actuated beam steering mirror is presented. It can be rotated about two perpendicular axes to steer an optical beam within an angular cone of up to 60° in vector scan mode with an angular resolution of 1 mrad and a response time of 300 ms. To achieve such angular performance relative to mirror size, the microassembly was performed from sub-components fabricated from 4 different wafers. To combine infrared detection with inertial sensing, an electroplated proof mass was flip-chipped onto a 256x1 pixel uncooled bolometric FPA and released using laser ablation. In addition to the micro-assembly technology, performance results of packaged devices are presented. Finally, to simulate a 3072x3 pixel uncooled detector for cloud and fire imaging in mid and long-wave IR, the staggered assembly of six 512x3 pixel FPAs with a less than 50 micron pixel co-registration is reported.

Keywords: heterogeneous assembly, uncooled bolometric FPAs, IR imaging, MEMS mirrors

1. INTRODUCTION

The growing market for low-cost, portable systems with complex functionality has opened up new avenues for miniaturization technologies. Unlike surface micromachined and monolithically fabricated MEMS devices, newer microsystems have grown significantly in design complexity and material heterogeneity. This trend has led the MEMS community to develop multi-die packaging of different functionalities or multi-technology (i.e. wafer) approaches to assemble and fabricate devices respectively [1]. This approach is commonly referred to as heterogeneous device assembly and integration. Over the years, INO has built a strong expertise in MEMS fabrication and packaging, in particular VO_x-based uncooled bolometric detectors [2;3] and integration of micro-optical components [4]. Based on this, the present paper demonstrates through three devices that heterogeneous integration can advantageously enable the fabrication of complex microsystems and overcome limitations of standard monolithic integration. First, the performance of a giant (e.g. about 3 mm in diameter), electrostatically actuated beam steering mirror is presented. For many civilian and defense applications requiring the manipulation of laser beams, current techniques used for laser beam steering are often based on mechanical devices such as rotating mounts and gimbals. Although they are relatively mature and widely used, these devices have shortcomings (inertia, sensitivity to vibrations, "fragility", etc.) that limit their performances. The developed MEMS-based mirror prototype can be rotated about two perpendicular axes to steer an optical beam within an angular cone of up to 60° in vector scan mode with an angular resolution of 1 mrad and a response time of 300 ms. To achieve such performance with a mm-size mirror of adequate flatness, the microassembly was performed from sub-components fabricated from 4 different wafers [5].
Second, to meet size, weight and power (SWAP) budget constraints of miniature satellites, a device combining infrared detection with inertial sensing is described. The integration of both functionalities was achieved by flip-chip bonding a proof mass to a 256x1 pixel uncooled bolometric FPA [6]. The accelerometer principle based on a proof mass acting as a

[1] Corresponding author : patrice.topart@ino.ca

mask suspended above a bolometer is demonstrated. The resulting accelerometer sensitivity (with the bolometer at atmospheric pressure) of 8.5 μV rms/g is consistent with the measured proof mass displacement of 7.6 μm/g. Finally, the staggered assembly of multiple uncooled 512x3 pixel FPAs [7] is demonstrated to achieve wide swath IR imaging capability. An overall die-to-die pixel co-registration less than the ±50μm requirement was obtained.

2. DUAL-AXIS MEMS-BASED MIRROR

2.1 Design, fabrication and assembly

The design and fabrication of this steering mirror have been described in detail in [5]. Finite element simulations using ANSYS modeling program were conducted to optimize the mirror design and determine the main characteristics to meet requirements. These included a rotation about two perpendicular axes to steer an optical beam within an angular cone of up to 60° with an angular resolution of 1 mrad, a high throughput in the mid-wave IR and a response time of a few hundred ms. The electrostatically actuated mirror is about 3 mm in diameter. Any beam pointing direction can be selected and maintained within this angular cone where arbitrary beam trajectory can also be defined. To achieve such performance while assembling various parts covering sizes from few tens of microns to millimeter, the heterogeneous assembly of parts fabricated on multiple wafers was conducted.

The device fabrication is based on high precision micro-assembly which relies on selective electroplating of Ni/Au, deep reactive ion etching (DRIE) of silicon and flip-chip bonding using a Fineplacer Pico (Finetech, Germany) with ±5 μm positioning accuracy. The fabrication process involved the assembly of 4 separate components, i.e. address electrodes, thick pedestal, gimbals structure and mirror plate. Single crystal silicon was used as structural material for the thick pedestal and mirror plate whereas nickel was selected for gimbals and hinges. Alumina was the substrate material for electrodes. Figure 1 shows the fabricated mirror parts.

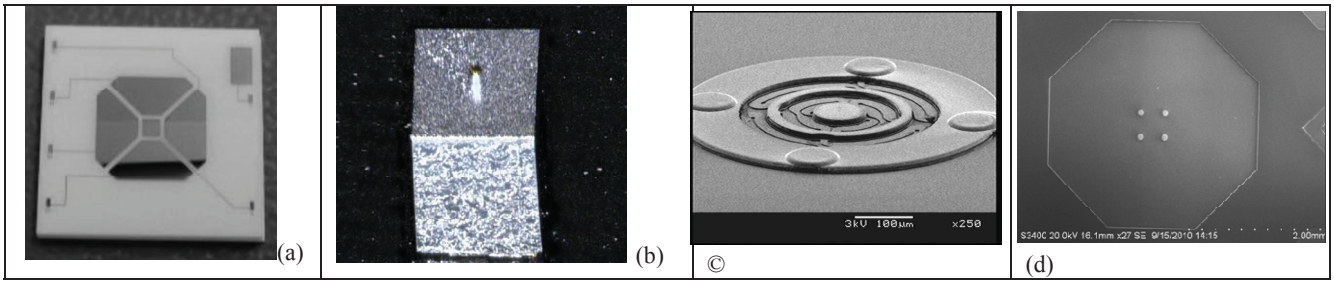

Figure 1: Mirror parts: a) Address electrodes on alumina chip, b) Thick pedestal equipped with Ni/Au stud, c) Nickel gimbals and serpentine hinges and d) Silicon mirror plate and the associated pedestals equipped with Ni/Au studs.

The die-level assembly process was divided in 3 main steps: first, assembly of thick silicon pedestal to electrode chip; second, bonding of gimbals onto thick pedestal followed by the release of their carrier wafer and third, bonding of the thin, metalized silicon mirror to gimbals followed by release of the sacrificial layer.
The flip-chip bonding of the thick silicon pedestal to the electrode chip involved the gold-rich eutectic $Au_{80}Sn_{20}$ alloy. Solder preforms of predefined shape were used. Prior to flip-chip assembly, plasma cleaning of the gold surface of the thick pedestal backside was achieved with O_2 and Ar gas mixtures. Then, the solder preform was accurately positioned on the electrode. The flip-chip bonding was then accomplished using a peak reflow temperature between 320°C and 350°C and a bond pressure in the range of 1 to 6 MPa. Such pressure level was low enough to avoid spilling out the solder from the bonding area. The soldering operation was performed in a non-oxidizing, nitrogen atmosphere. The thick silicon pedestal bonded to the electrode chip is shown in Fig. 2a.

Before carrying out the second assembly of gimbals built on a carrier wafer, a sacrificial layer was inserted to support the gimbals during the flip-chip assembly of mirror plate. Temperature and pressure are key parameters determining the quality of the thermocompression bonding of metal joints. The optimization of these parameters was crucial when assembling these fragile components having very thin geometries. Co-planarity, alignment tolerance and parallelism

adjustments were also very important to achieve good gold to gold thermocompression flip-chip bonding results. This assembly was carried out with particular care in minimizing the applied force to avoid damaging the structures. Prior to bonding, plasma cleaning of parts was conducted in an O_2 and Ar gas mixture. The process was performed in N_2 atmosphere with bond temperature ranging between 200°C and 280°C and pressure from about 100 MPa to 150 MPa. Finally, de-bonding of carrier wafer was carried out.

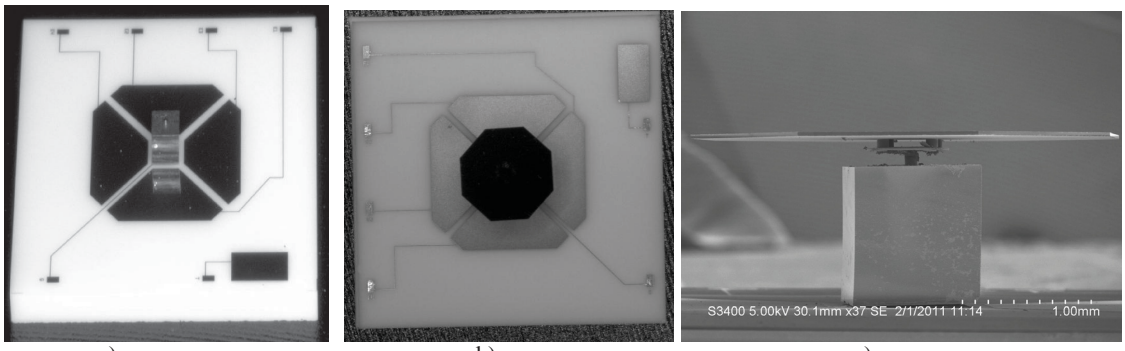

a) b) c)

Figure 2: Mirror assembly a) thick pedestal assembled to the electrode chip, b) top view of assembled device, c) final release of mirror device.

Prior to the third assembly of mirror plate to the gimbals, the carrier substrate supporting the mirror plate was first released by etching the temporary waferBOND™ coating using the waferBOND™ remover. By design, a mirror thickness of 30 μm was chosen to allow for safe mirror plate handling during assembly while maintaining surface flatness after assembly. This gold to gold bonding was carried out using a temperature ranging between 200°C and 280°C and pressure in the range of 50-150 MPa, Fig. 2b. The mirror was then released, Fig. 2c.

2.2 Packaging

The package header consisted of a COTS kovar package compatible with high voltage operation. Epoxy adhesives were used for attaching the chip to the header, which was wirebonded using gold ball bonding. Hermetic package sealing was accomplished in N_2 atmosphere using an AR-coated CaF_2 window. The hermetic sealing of the package is required to protect the device against the external environment (prevent moisture, electrically charged species and other contaminants) and keep an inert atmosphere inside the package. The sealed package was then integrated to a printed circuit board (*PCB*) by direct soldering of package pins onto the *PCB,* Fig. 3a. Final integration of the package soldered to the PCB with a thermoelectric cooler (TEC) and coaxial cables was finally achieved using a custom designed and fabricated housing, Fig. 3b.

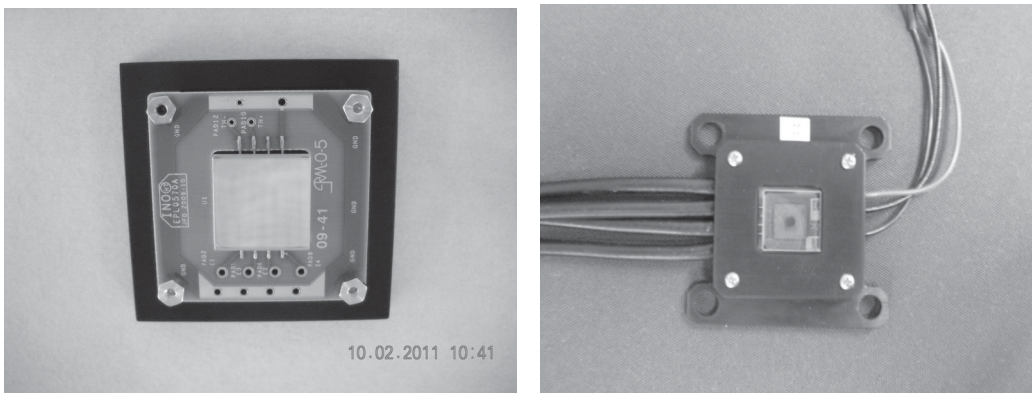

a) b)

Figure 3: Mirror housing module: a) Package pins soldered to the PCB, b) Device module in its final assembly state.

2.3 Device characterization

The mirror characterization included the measurement of the angle vs voltage responses, the steering module throughput, the response time and the pointing stability and accuracy. The setup shown in Figure 4 was used to measure all beam steering mirror characteristics reported below except the throughput. It included a camera, a He-Ne laser, attenuation filters, folding mirrors, the micromirror under test (MUT) and the observation plane. The MUT was aligned so that the beam reflected by the non-activated steering mirror was perpendicular to the observation plane. The incidence plane defined by the non activated mirror (the initial incidence plane) was horizontal.

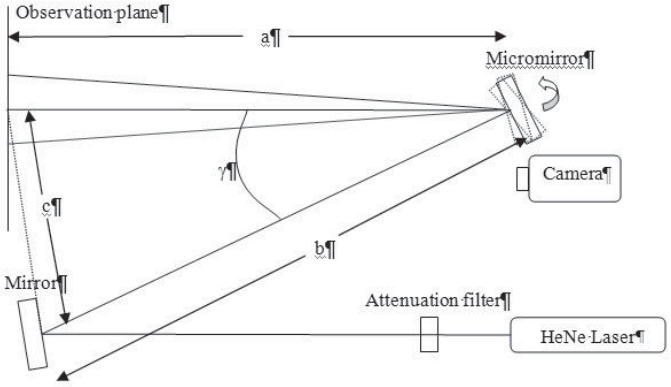

Figure 4: Micromirror characterization setup.

The static response of a beam steering mirror prototype was determined following the activation of each of the four electrodes separately, Figure 5. Both optical and mechanical angles are shown. The opposite electrodes E1 and E2 (Fig. 2a rotate the mirror around the outer axis of the gimbals, whereas E3 and E4 rotate the mirror around the inner axis. For electrodes E1 and E2 that rotate the mirror normal to the initial incidence plane, it can be shown that, under our experimental conditions, the optical angles must be divided by 1.89 to obtain the mechanical angles. The higher tilt angles before pull-in extracted from Figs. 5a and 5b are summarized in Table 1.

Table 1: Maximum angles reached by the beam steering mirror prototype.

	Optical angle(°)	Mechanical angle (°)
Activation of E1	18.10	9.57
Activation of E2	-19.39	-10.23
Activation of E3	-25.05	-12.52
Activation of E4	28.60	14.30

In addition, the data of Figs. 5 indicate that no significant hysteresis is observed in the static response of the device. Also, increasing or decreasing the voltage to reach a target value did not affect significantly the resulting mirror position, Figure 5.

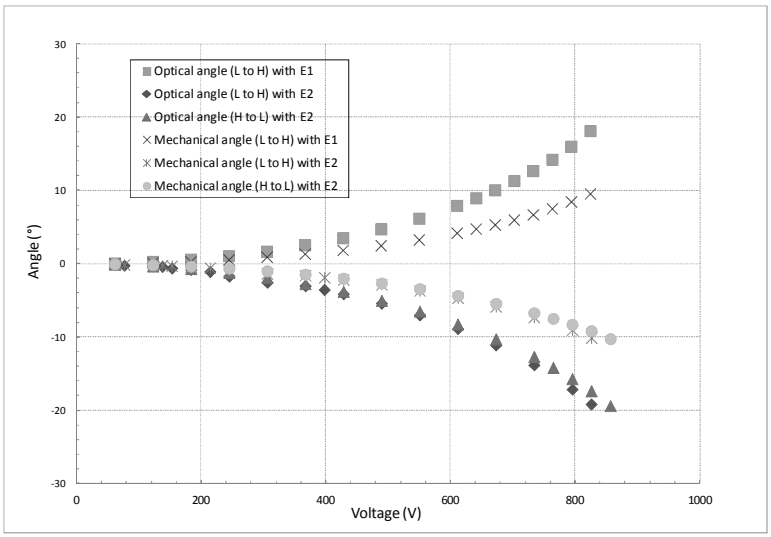

(a)

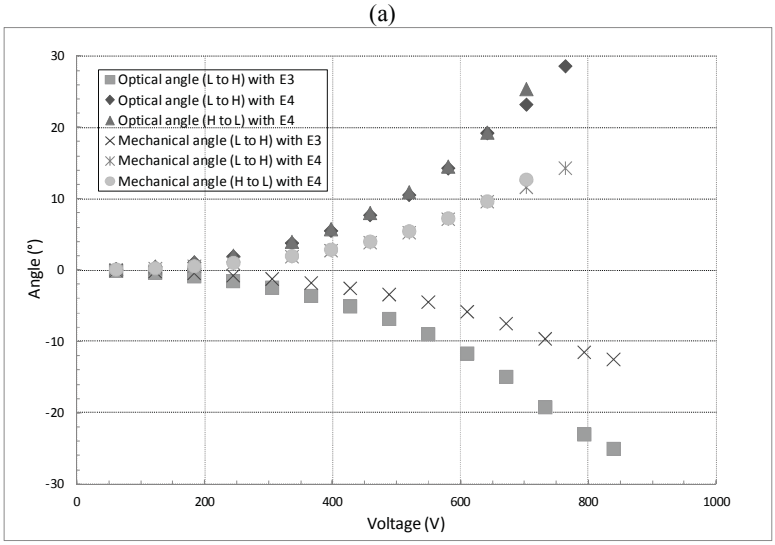

(b)

Figure 5: Static response of beam steering mirror prototype, a): activation with electrodes E1 and E2 (outer axis), b): activation with electrodes E3 and E4 (inner axis). L to H and H to L mean that the voltage was increasing and decreasing, respectively. Both optical and mechanical angles are provided.

The response time of the device was also determined using the setup of Fig. 4. The voltage waveform used to activate the mirror was a half sine wave with a period that was adjusted by changing the number of intermediate voltage values included in the waveform. Up to 400 intermediate voltages values could be used to define this waveform. Each intermediate voltage value used in the waveform definition increased the waveform duration by 1 ms. The response time was then estimated knowing the starting time of the activation which corresponded to the beginning of the voltage waveform and the activation ending time given by the time at which the signal of a detector located at the known arrival position of the optical beam was stabilized. Among all tested waveform durations, the waveform duration of 300 ms seems to have rotated the mirror in a quasi-static way which resulted in a device response time of about 300 ms similar to the activation waveform duration, Fig. 6. This response time was of the same order of magnitude as that estimated from transient finite element analysis [5].

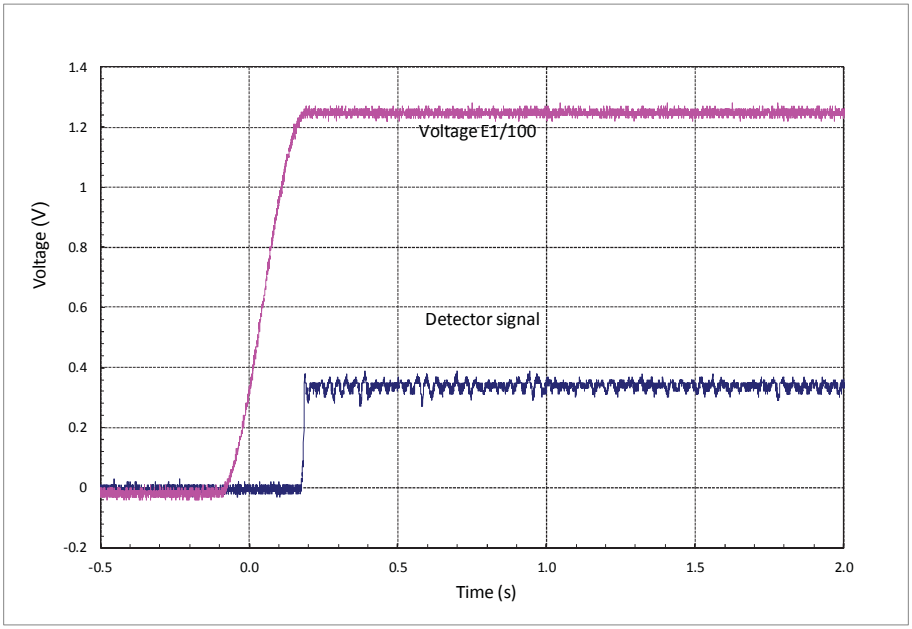

Figure 6: Time dependence of the voltage waveform (divided by 100) applied to electrode E1 and of the corresponding detector signal for a waveform duration of 300 ms.

The pointing stability and accuracy of the steering device was verified. This was tested by sending commands to the mirror corresponding to a set of four selected pointing directions at the beginning of the test and after 1 and 2 hours of operation. The resulting reflected beam directions were compared to evaluate the device accuracy and stability with time. One test was performed with relatively low voltages of 306 V and 229.5 V for either electrode E1 or E2 and E3 or E4, respectively. All pointing directions were relatively stable and accurate with errors going from 0.5 to 1.5 mrad. Errors on the initial position of the deactivated mirrors were about 0.5 mrad in all cases. The errors were calculated using the beam positions at the beginning of the test as a reference. Another test was performed with higher voltages applied to the control electrodes (459 V applied to either electrode E1 or E2, and 612 V applied to either electrode E3 or E4). For this test however, the results were not as good as those obtained for the test performed with lower voltage values. Typical errors on the pointing directions obtained for higher voltages range from 0.7 to 4.5 mrad with a mean value of 2.8 mrad. In general, the errors measured after 1 hour of operation did not seem to be significantly different those measured after 2 hours.

The optical throughput in the spectral range from 2 to 5 µm which depended on beam interception factor, mirror reflectivity and window transmittance was evaluated to be close to 85%, uniform within ± 10%.

In summary, fabrication and assembly processes were developed to manufacture an electrostatically actuated dual axis mm-sized MEMS mirror. The fabrication process combined surface and bulk micromachining. Flip-chip assembly of individual mirror parts was based on AuSn preform soldering as well as Au-Au thermocompression bonding. The performance of packaged devices was determined. A maximum mechanical angle of 14.3º was obtained for an actuation voltage of about 850V. The response time of the mirror was about 300ms. The optical throughput in the spectral range from 2 to 5 µm including beam interception factor, mirror reflectivity and window transmittance was evaluated to be close to 85%, uniform within ± 10%. The pointing stability and accuracy of the steering device were such that errors going from 0.5 to 1.5 mrad were obtained at lower applied voltages, whereas a mean error value of 2.8 mrad was obtained at higher voltages.
Despite the important thickness of the silicon mirror (30 µm), a slight bump typically appeared at the mirror center after mirror/gimbal assembly. Although not very obvious, this defect still had a significant impact on the quality of the reflected beam profile. Future improvements should include the elimination of this defect.

3. COMBINED ACCELEROMETER-MICROBOLOMETER

In many applications, the control of spacecraft's attitude and orbit can be accomplished using a horizon sensor in combination with an inertial measurement unit (IMU) and a GPS. However, the total SWAP budget of these combined discrete sensors will not likely meet requirements of microsatellites. Thus, to improve system accuracy and dynamic range, reduce SWAP budget and increase reliability, a new concept for an IMU embedded in a miniature horizon sensor was proposed. In this work, the proof of concept for the integration of an accelerometer into a horizon sensor is presented, Fig. 7. The latter consists of a linear array of microbolometers e.g. a 256x1 pixel FPA with a pixel pitch of 52 μm [8]. The accelerometer principle relies on the change of the bolometer signal induced by a proof mass connected to the substrate by springs and which masks to a variable extent the bolometric detectors located underneath depending on its position. The proof mass position being related to the acceleration of the device, the signal of the partly masked bolometers provides a way of measuring this acceleration.

3.1 Design, fabrication and assembly

An heterogeneous integration approach was selected to integrate the proof mass onto the linear array of uncooled 256x1 pixel FPAs. This allowed to use known good bolometer dies and eliminated issues with the release of suspended bolometer structures at the end of a standard monolithic process. Nickel, having a Young's modulus of 186 GPa, was selected for the structure since it has a large density, yield stress and can be electroplated easily. Finite element analysis (FEA) using ANSYS software led to the design of micromechanical devices with proof masses moving in the range of 7 to 20 μm upon a steady state acceleration of 1g (9.8 m/s^2) applied in the longitudinal direction (parallel to the bolometer linear array). For a given design, this displacement strongly depends upon nickel springs width and length.
The design of the connecting springs is particularly important since they must allow large proof mass displacements, such as those mentioned above, in a longitudinal direction. Additionally, they must limit this displacement in the lateral direction (parallel to the substrate and perpendicular to the array) to minimize the cross-axis sensitivity. Finally, since the proof masses are suspended on top of the bolometer pixels, the springs must also limit this displacement in the vertical direction (perpendicular to the substrate) to prevent any contact between the proof masses and the bolometers., Typical lateral and vertical proof mass displacements of about 1 μm and 5 μm respectively were calculated. These results indicated that the transversal spring rigidities were sufficient to prevent any damage of the bolometer. Moreover, simulations confirmed that upon motion of the proof mass, stresses would not exceed 10 MPa, well below the yield stress. Designs of apertures in the proof masses for 52 μm pitch microbolometers were such that along the longitudinal and lateral directions, two half neighbouring bolometers were covered.

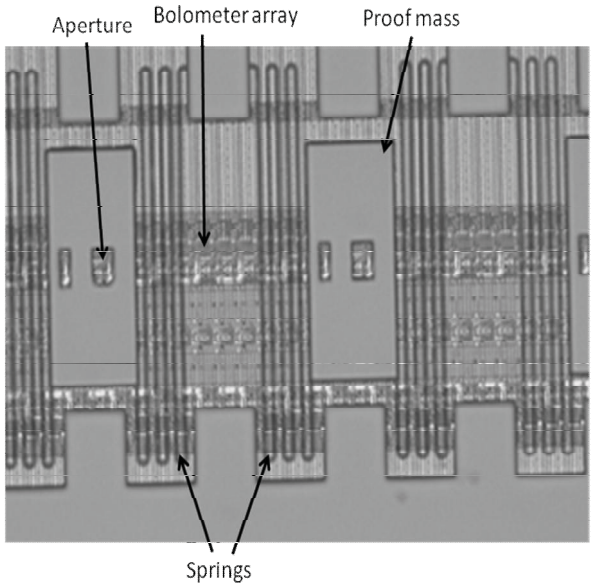

Figure 7: Picture of the device exhibiting nickel proof masses equipped with apertures, the linear bolometer array and nickel springs. Nickel spring length is typically 0.84 mm.

Apertures were aligned with the center of bolometer pixels which provides maximum sensitivity. A borofloat glass wafer was first covered by a polyimide sacrificial layer and a gold seed layer. Thus, the proof masses and springs were electroplated on this separate glass wafer from a nickel sulfamate bath. The applied plating current was adjusted to maintain an internal stress within +/- 5 MPa for 25 µm-thick layers. Nickel springs had a thickness and width of 6 and 4 microns respectively while the proof mass had a thickness of 46 microns and length of 500 µm, Fig. 7. A spacer made of the negative tone resist KMPR also serving as permanent bonding layer to bolometer chip was patterned on top of nickel. The bolometer chip was attached and wirebonded to a ceramic PGA package equipped with a ceramic routing circuit. Accelerometer chips from the borofloat wafer were flip-chip bonded onto the microbolometer chip using KMPR as spacer/permanent bonding layer. Bonding temperature and force was less than 250°C and 15N respectively. Alignment was performed using pads of the 256x1 pixel FPA and the KMPR spacer.

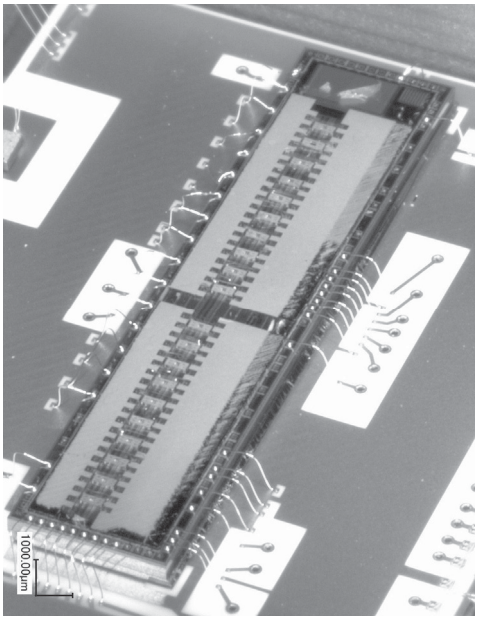

Figure 8: Picture of the device before release of glass carrier wafer.

Finally, the borofloat glass carrier wafer was released using laser ablation of the sacrificial layer [9]. To that end, a setup based on a tripled YAG laser operating at 355 nm was developed. The package was placed on an automated XY stage so that laser ablation parameters of polyimide could be optimized. After removal of the glass carrier wafer, polyimide residues were removed by ashing in an oxygen plasma. We found that a good adhesion between the thin nickel springs and the gold seed layer was essential for the device mechanical integrity during laser ablation. A picture of the assembly before glass wafer release is shown in Fig. 8.

3.2 Device performance

Both the displacement of the proof masses and the variation of bolometers signals were measured in response to the acceleration applied to the device. The acceleration was varied by changing the angle between the gravity acting vertically and the main translation axis of the proof masses which corresponds with the longitudinal axis of the bolometer linear array. This was done with a goniometer on which the device was mounted, Fig. 9a. This way, the projection of the force acting on the proof masses along their main translation axis changes as the cosine of the angle which allows the investigation of the accelerometer response over an acceleration range from -1g to +1g. Displacement was measured using a microscope Keyence VHX-1000 with tiltable objective taking the KMPR/nickel anchor as reference, Fig. 9b.

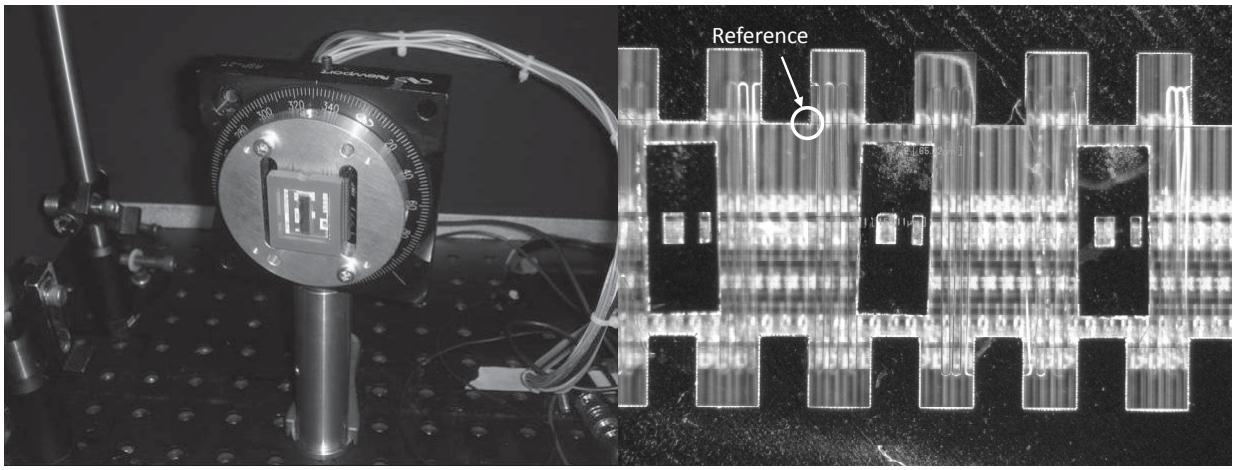

(a) (b)

Figure 9. (a) Picture of device packaged in ceramic header and mounted on goniometer. (b) Typical image obtained for the proof mass position measurement. The white circle has been added to the image to indicate the corner of the KMPR/nickel anchor used as the reference for the displacement measurements.

Bolometer signals presented below were measured at atmospheric pressure. The temperature of the black body used to illuminate the bolometers was set to 500°C (773 K) in order to increase substantially the radiation intensity and somewhat compensate for the loss of signal due to the atmospheric pressure operation. In addition, the bolometer signal was modulated at 100 Hz by varying the incident radiation intensity with an optical chopper. This allowed the use of a heterodyne bolometer signal detection scheme involving a lock-in amplifier. The test setup allowed for reading-out the signal from any bolometer from the array using a Labview program.

The typical displacement of a proof mass (#13) as a function of the acceleration along the longitudinal axis (X-axis) is shown in Fig. 10. The response exhibits some non linearity indicating that the springs linking the mass to the nickel/KMPR anchors do not strictly follow Hooke's law. The linear fit gives a slope of 7.6 μm/g, This is somewhat lower than the simulated values of about 10 μm/g. This may be attributed to deviations of nickel properties and actual dimensions as compared to simulated values.

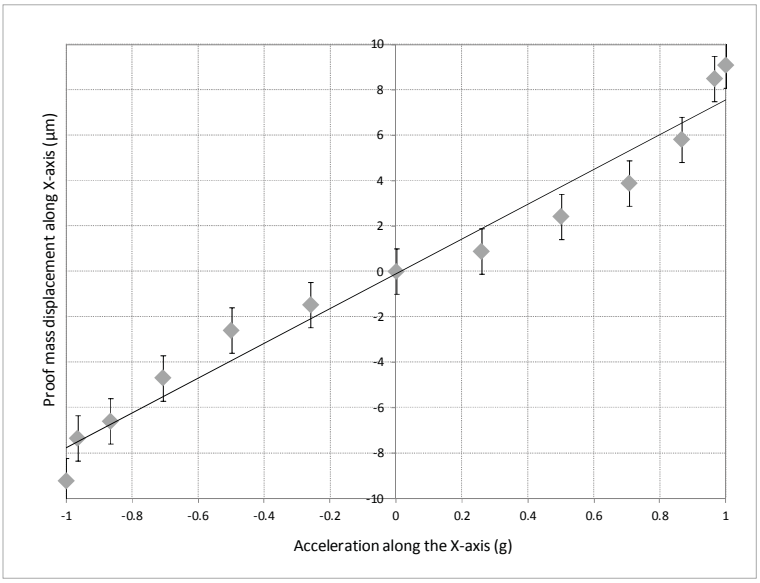

Figure 10: Displacement of proof mass #13 as a function of the acceleration along the longitudinal direction.

The dependence of the bolometer signal (measured in air, at atmospheric pressure) on acceleration is shown in Fig. 11. The sensitivity of the accelerometer is about 8.5 µV rms/g. From the measured displacement of 7.6 µm/g, a variation of the bolometer signal of about 15 %/g would have been expected considering the pixel length of 50 µm. This discrepancy may be explained by a misalignment of the proof mass with respect of the bolometer, the effect of the non responsive bolometer legs and non uniform response of the bolometer.

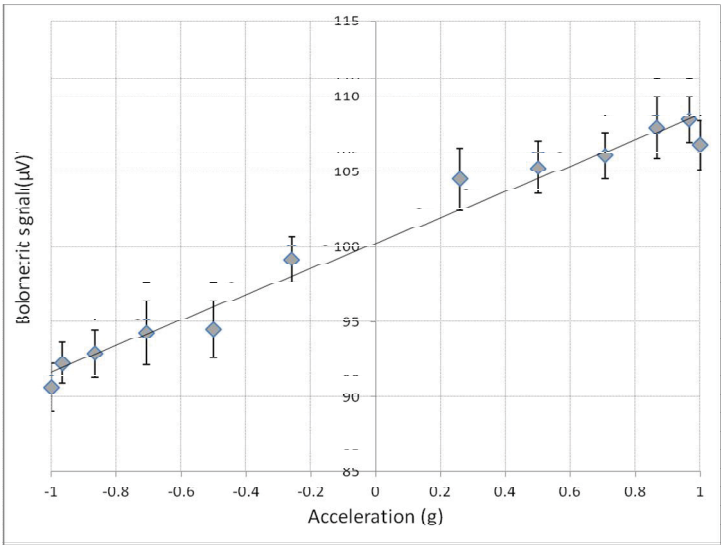

Figure 11: Bolometric signal corresponding to the displacement of proof mass #13 as a function of the acceleration along the X-axis; (sample reference Pk3- D223-BF34)

In summary, the accelerometer principle based on a proof mass acting as a mask suspended above a bolometer has been demonstrated. The mechanical response (7.6 µm/g) to acceleration along the main translation or longitudinal axis (X-axis) of the proof mass is relatively close to the estimated response based on ANSYS simulations (10 µm/g). The mechanical response to acceleration along the lateral direction (perpendicular to the proof mass main translation axis)

could hardly be characterized with the available measurement precision and seems minimal as expected. The proof mass displacement is symmetric with respect to an X-axis/gravity angle of 180°, as expected. No hysteresis could be detected in the displacement of the proof mass. The measured relative variation of the bolometer signal as a function of acceleration was lower than estimates based on the measured proof mass displacement. This can most probably be explained by various interrelated factors: alignment of the proof mass with respect of the bolometer, effect of the non responsive bolometer legs and non uniform response of the bolometer.

4. STAGGERED ASSEMBLY OF 512X3 PIXELS BOLOMETRIC FPAS

A number of space agencies identified missions that would benefit from compact, uncooled, multi-spectral wide-swath IR cameras. In this context, INO was approached to design, manufacture and test a multi-FPA detector for a spaceborn application. In order to achieve mission goals, it was necessary to achieve a die-to-die pixel co-registration of less than 50 µm while assembling multiple dies in a close to 16 cm-long package. The INO IRL512 appeared as a suitable candidate FPA for such a detector in that it featured three lines of 512, VO_x-based microbolometer pixels, with a pixel pitch of 39µm and a line spacing of 2.88 mm. Indeed, on a low-earth orbit (LEO), the 39µm pixel size translates into a ~300m ground spot, which is suitable for most missions. Moreover, the 2.88 mm line spacing provides enough room to place a spectral bandpass filter in front of each pixel line while achieving minimal line-to-line crosstalk.

4.1 Microassembly

Six IRL512 FPAs were integrated in a staggered configuration onto a routing circuit placed in a large metallic header, as shown in Fig. 12a. The spectral bandpass filters were mounted on the detector cover, as shown in figure 12b. In order to maximize filter-coatings coverage, the filters were manufactured using the "butcher-block" technique. The gap between the focal-plane and the internal face of the filters was kept minimal. The footprint of the package was 157 mm X 77 mm. The height of the package, including the cover, was 16 mm.

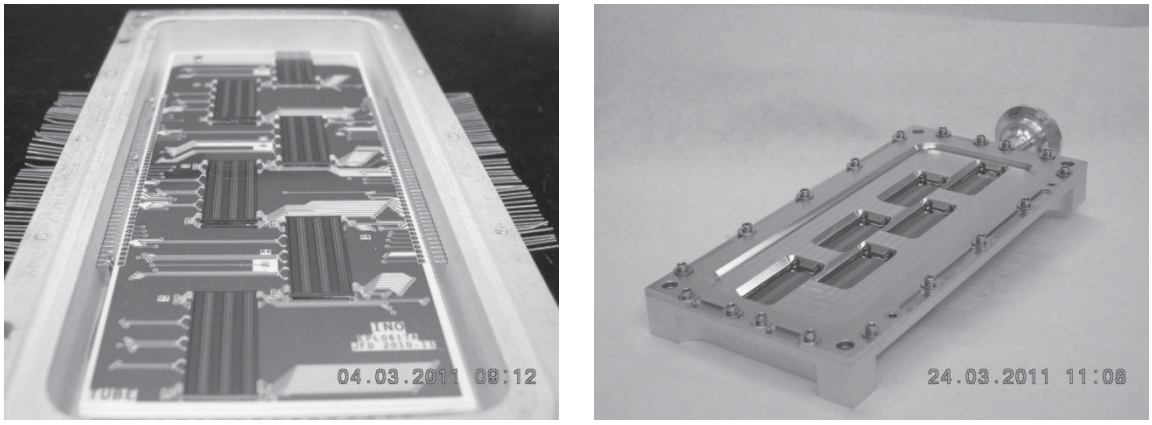

a) b)

Figure 12: The header subassembly showing the 6 staggered IRL512 512x3 microbolometer FPAs (a) and the complete detector package showing the bandpass filters/windows (b)

The key element that enabled accurate co-registration of the dies was the ceramic thin-film routing circuit. An extensive market survey was performed to find a qualified partner having the ability to manufacture large 50mm x 122mm single-piece thin film routing circuits onto which the dies were attached by flip-chip bonding using epoxy. Alignment was performed using alignment marks placed on the routing circuit and edges of the dies. The routing circuit itself was aligned with a mechanical jig with respect to the dowel pins in the header. The cover was aligned with respect to dowel pins present in the header. To reduce the misalignment between the dies and optical filters, the pockets in the cover which received the optical filters were machined once the die-to-die pixel co-registration measurement has been completed. Optical filters for each line of microbolometers were aligned in the pockets mechanically.

4.2 Determination of die-to-die pixel co-registration

The die-to-die pixel co-registration was measured, Fig. 13. Each diamond shown in the graph represent an actual measurement. The line is the least-square fit of all the measurements. The co-registration error was evaluated as the orthogonal distance from the line to each diamond, and is reported in the table 2.
Negative numbers mean that the diamond is below the line while positive numbers denotes diamonds above the line.

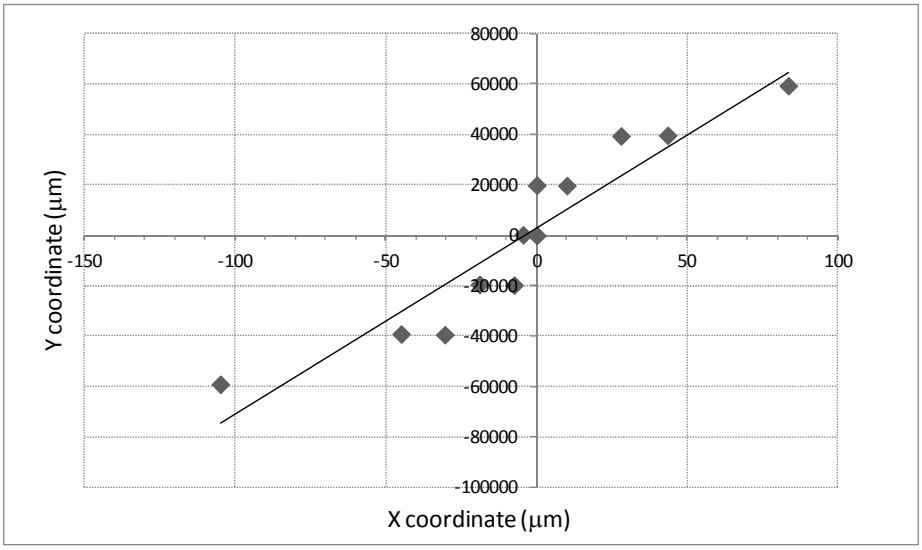

Figure 13: Die to die pixel co-registration: X, Y coordinates of pixels on the six 512x3 pixel FPAs

Table 2: Die to die pixel co-registration error calculated from Fig. 13

FPA number	FPA corner	Error (µm)	FPA number	FPA corner	Error (µm)
Die 1	Top right	20.750	Die 4	Top right	-4.045
Die 1	Bottom left	-12.186	Die 4	Bottom left	23.016
Die 2	Top right	-27.021	Die 5	Top right	12.720
Die 2	Bottom left	-11.455	Die 5	Bottom left	6.283
Die 3	Top right	-23.292	Die 6	Top right	21.449
Die 3	Bottom left	0.771	Die 6	Bottom left	-6.991

These results show that seven out of the twelve error numbers were below 13µm, meaning that very accurate co-registration was achieved after assembly. The overall co-registration was -27µm / +23µm, which is well within the ±50µm requirement.

5. CONCLUSION

In this paper, the performance of three MEMS devices integrating either large parts of dissimilar sizes and materials, a combination of microsystems with different function or multiple dies was described. This was achieved using an heterogeneous assembly and integration approach. Performance testing of packaged, electrostatically actuated dual axis mm-sized MEMS mirror revealed that a mechanical angle of 14.3º could be obtained for an actuation voltage of 850V.

The response time of the mirror was about 300ms. The optical throughput in the spectral range from 2 to 5 µm was close to 85%, uniform within ± 10%. The pointing stability and accuracy of the steering device were such that errors going from 0.5 to 1.5 mrad were obtained at lower applied voltages, whereas a mean error value of 2.8 mrad was obtained at higher voltages.
The proof of concept for an accelerometer principle based on a proof mass acting as a mask suspended above a bolometer was demonstrated. The integration of these functions in a single device could open the door for sensing in miniaturized systems such as horizon sensors for space applications. The mechanical response (7.6 µm/g) to acceleration along the main translation axis (X-axis) of the proof mass was fairly close to that estimated by ANSYS simulations. This was reflected by a measured variation of the bolometer signal as a function of acceleration of 8.5 µV rms/g.
Finally, the staggered assembly of six 512x3 pixel uncooled FPAs in a large package exhibited a die-to-die pixel co-registration compliant with requirements. This resulted in a 3072x3 pixel uncooled FPA with IR imaging capability in various IR bands and swath coverage of 1000 km or more.

REFERENCES

[1] M. Lapisa, G. Stemme, F. Niklaus, “Wafer-level heterogeneous Integration for MOEMS, MEMS and NEMS”, IEEE Journal of Quantum Electronics, Vol. 17, 629-644 (2011)
[2] A. Paquet, S. Deshaies, Y. Desroches, J. Whalin and P. Topart, “Influence of ceramic package internal components on the performance of vacuum sealed uncooled bolometric detectors”, Proc. SPIE 8614 (2013)
[3] F. Genereux, J.-E. Paultre, B. Tremblay, F. Provençal, C. Alain, “Influence of Pixel Geometry on the 1/f Noise Coefficient”, Proc. SPIE 8704 (2013)
[4] S. Garcia-Blanco, P. Topart, S. Leclair, J.-S. Caron, H. Jerominek, “3D MOEMS-based optical micro-bench platform for the miniaturization of sensing devices”, Proc. SPIE 6887 (2008).
[5] S. Ilias, F. Picard, K. Le Foulgoc, J. Osouf, C. Larouche, J-S. Caron, P. Topart, S. G. Blanco, D.Vincent, J. F. Lepage, B. Gilbert, "Large diameter dual-axis MEMS-based mirror for laser beam steering", Proc. SPIE 7930 (2011).
[6] L.Ngo. Phong, K. Yoshihara, F. Chateauneuf, “JC2Sat & Mirad: A unique nanosatellite with a unique EO payload”, International Astronautical Federation -59th International Astronautical Congress IAC, 6, pp. 3841-3850, (2008).
[7] L. Ngo Phong, O. Pancrati, L. Marchese, F. Chateauneuf, “Spaceborne linear arrays of 512x3 microbolometers”, Proc. SPIE 8614 (2013).
[8] T.D. Pope, H. Jerominek, C. Alain, F. Cayer, B. Tremblay, C. Grenier, P. Topart, S. Leclair, F. Picard, C. Larouche, B. Boulanger, A. Martel, Y. Desroches, “Commercial and custom 160x120, 256x1 and 512x3 pixel bolometric FPAs”, Proc. SPIE, 4721, 64-74 (2002).
[9] R. Guerre, U. Drechsler, D. Jubin, and M. Despont, "Selective transfer technology for microdevice distribution", IEEE Journal of Microelectromechanical Systems, Vol. 17, Issue 1, 157-165 (2008).